TECHNISCHE UNIVERSITÄT
KAISERSLAUTERN

SCHRIFTEN ZUR

FUNKTIONALANALYSIS UND GEOMATHEMATIK

Thorsten Maier

Wavelet-Mie-Representations for Solenoidal Vector Fields with Applications to Ionospheric Geomagnetic Data

Bericht 7 – Januar 2004

FACHBEREICH MATHEMATIK

Wavelet-Mie-Representations for Solenoidal Vector Fields with Applications to Ionospheric Geomagnetic Data*

Thorsten Maier

TU Kaiserslautern
Geomathematics Group
67653 Kaiserslautern
P.O. Box 3049
Germany

phone:	++49 631 205-4584
fax:	++49 631 205-4736
email:	tmaier@mathematik.uni-kl.de
www:	http://www.mathematik.uni-kl.de/∼wwwgeo

Abstract

A wavelet technique, the wavelet-Mie-representation, is introduced for the analysis and modelling of the Earth's magnetic field and corresponding electric current distributions from geomagnetic data obtained within the ionosphere. The considerations are essentially based on two well-known geomathematical keystones, (i) the Helmholtz-decomposition of spherical vector fields and (ii) the Mie-representation of solenoidal vector fields in terms of poloidal and toroidal parts. The wavelet-Mie-representation is shown to provide an adequate tool for geomagnetic modelling in the case of ionospheric magnetic contributions and currents which exhibit spatially localized features. An important example are ionospheric currents flowing radially onto or away from the Earth. To demonstrate the functionality of the approach, such radial currents are calculated from vectorial data of the MAGSAT and CHAMP satellite missions.

AMS Classification. 42C40 , 65Z05 , 86A25

Key words. Mie-representation, Helmholtz-decomposition, Vectorial Wavelets, Geomagnetic field modelling

*This work was supported by the priority program "Geomagnetic Variations" of the German Research Foundation (DFG FR 761/10-1)

1 Introduction

Macroscopic electrodynamics is the theoretical basis for dealing with the subject of satellite magnetometry in geomagnetism. The fundamental equations governing that branch are Maxwell's equations for polarizable media. Since typical timescales in satellite magnetometry are of the order of days and typical lengthscales are of the order of the Earth's radius, the typical system velocities are much smaller than the speed of light and therefore the quasi-static (or stationary) approximations of Maxwell's equations (i.e. the pre-Maxwell equations) can be used (cf. e.g. [2]). As far as the magnetic field is concerned, these equations read:

$$\begin{aligned} \nabla \cdot b &= 0, \\ \nabla \wedge b &= \mu_0 j, \end{aligned}$$

where b (in classical geophysical notation usually denoted by $\vec{B}$) is the magnetic induction, i.e. the magnetic field, j is the electric current density and μ_0 is the vacuum permeability, $\mu_0 = 4\pi \cdot 10^{-7}\mathrm{VsA}^{-1}\mathrm{m}^{-1}$. Note that, in this approximation, the electric current density j is also of zero divergence, i.e.

$$\nabla \cdot j = 0.$$

Many concepts in geomagnetic modelling assume that the geomagnetic data are solely collected within a spherical shell $\Omega_{(R_1,R_2)}$ around the origin – with inner radius R_1 and outer radius R_2 – between the Earth's surface and the ionosphere so that the current density j can be neglected. This results in $\nabla \wedge b = 0$, $\nabla \cdot b = 0$ which implies that there exists a scalar potential U in $\Omega_{(R_1,R_2)}$ such that $b = -\nabla U$ and $\Delta U = 0$ in $\Omega_{(R_1,R_2)}$. In order to model the magnetic field b the potential is expanded into a Fourier series of (scalar) spherical harmonics and the expansion coefficients are chosen such that the gradient of the potential fits – in the sense of a least–square metric – the given vectorial data as good as possible. This method, which is known as Gauss representation, has been used and constantly improved for more than 150 years now, so that profound numerical and theoretical techniques are existent (see e.g. [23]).

Satellite missions (like MAGSAT, Oersted, CHAMP) collect their data *within* the ionosphere. Due to the intense solar radiation on the Earth's dayside (i.e. the hemisphere directed to the sun) the electric conductivity of the ionosphere is increased and tidal forces, due to solar heating as well as solar and lunar attraction, can drive large electric current systems. Among the most important ionospheric current systems are the so-called equatorial electro jet (EEJ) and the polar electro jets (PEJ), as well as the so-called field aligned currents that are flowing radially towards and away from the geomagnetic poles. In connection with polarization effects in the ionospheric plasma the geomagnetic field produces an enhanced hall conductivity (Cowling Effect) in the vicinity of the geomagnetic equator. This increased conductivity results in an amplified current system - the EEJ - flowing roughly along the magnetic equator. As regards our later considerations it is worth mentioning that the EEJ, though mainly tangential, also provides a notable radial current density which is known as the radial contribution of the meridional current system of the EEJ. The PEJ is mainly due to an increased conductivity and large horizontal electric field contributions in the polar ionosphere. Currents flowing along the geomagnetic field lines - the field aligned currents - are caused by magnetospheric and ionospheric coupling or imbalances of Sq-current systems (see e.g. [29] and the references therein). In the polar

regions field aligned currents flow onto or away from the Earth's body, thus contributing large radial current densities confined to these areas. The radial currents and the resulting magnetic effects, as well as the corresponding modelling approaches, are more and more subject of recent research (see, for example, in chronological order, [30], [34] , [9], [23], [29], [11], [4], [27], [31] and [35]). The numerical examples presented in this article also deal with the determination of such radial ionospheric currents from geomagnetic vectorial satellite data.

Due to the electric currents, the magnetic field measured by satellites in the ionosphere is no longer a gradient field anymore. In fact, it also contains magnetic contributions from current densities on the satellite's track. But this means that new vectorial methods, not based on the existence of a scalar potential, must be derived in close orientation on a (quasi–static) formulation of Maxwell's equations. The authors of [1, 2, 18, 34] suggest the resolution of the magnetic field by means of the Mie representation as an adequate replacement of the Gauss approach. The Mie representation, i.e. splitting the magnetic field into poloidal and toroidal parts, has the advantage that it can equally be applied in regions of vanishing as well as non-vanishing electric current densities. The poloidal fields are due to toroidal current densities below and above the satellite's track, whereas the toroidal fields are created by the radial currents which are crossing the satellite's orbit. It is this characteristic that makes the Mie approach a powerful tool for dealing with geomagnetic source problems, i.e. the problems of calculating magnetic effects due to given electric currents (direct source problem) and – vice versa – determining those current distributions that produce a predefined magnetic field (inverse source problem).

There remains the question of how to computationally obtain, in terms of suitable trial functions, the Mie-representation from a given set of vectorial data. Most of the considerations in [1, 2] and all the results in [11, 25, 29] are based on a spherical harmonic parametrization, i.e. starting point of the considerations are expansions of the poloidal and toroidal scalars in terms of spherical harmonics. On the one hand, this approach is advantageous since it admits the possibility to incorporate radial dependencies of magnetic fields and electric currents in a natural way. On the other hand, the global support of the spherical harmonics limits the practicability of this technique since it cannot cope with electric currents (and corresponding magnetic effects) that vary rapidly with latitude or longitude, or that are confined to certain regions. In fact, Backus [1] states that is might be advantageous to find a field parametrization in terms of functions that take efficient account of the specific concentration of the current densities in space. The uncertainty principle (confer the scalar theory by Freeden and Windheuser [17] and their generalization to the vector case by Beth [5]) provides an adequate tool for the classification of (spherical restrictions of) poloidal and toroidal vector fields by determining a trade off between two 'spreads', one for the position (space) and the other for the momentum (frequency). The main statement is that sharp localization in space and in frequency are mutually exclusive. The varieties of space/frequency localization can be illustrated by considering different poloidal and toroidal trial fields on the sphere being suitable for constructive approximation. Vector (spherical) harmonics show an ideal frequency localization, but no space localization. The spectrum of (band–limited and non band–limited) kernel functions known from harmonic and vectorial spline theory (cf. [12], [33], [14], [15]) shows all intermediate cases of space/frequency localization. But in view of the amount of space/frequency localization it is also worth distinguishing bandlimited from non–bandlimited kernels. As a matter of fact, it turns out that non–bandlimited kernels

show a much stronger space localization than their comparable band–limited counterparts. Roughly spoken, this is due to the fact that bandlimited kernels can be represented as finite sums of polynomials and therefore – though strongly smoothed compared to polynomial functions – tend to oscillate. In contrast, non-bandlimited kernels cannot be displayed as finite sums of polynomials and hence yield a stronger space localization. Finally, the Dirac kernels show ideal space localization, but no frequency localization. Thus they provide the final stage in the spatial resolution of the magnetic field by trial functions. In conclusion, vector harmonics and Dirac kernels are 'extreme trial functions' for purposes of geomathematical modelling. These facts help us to find a suitable characterization and categorization of the trial functions for modelling and approximation: Fourier methods (in terms of scalar/vector spherical harmonics, for example) are the canonical starting point to obtain an approximation of low frequency contributions (global modelling), while band-limited kernel functions can be used for the intermediate cases between long and short wavelengths (global to regional modelling). Due to their extreme space localization, non-bandlimited kernels can be utilized to deal with short wavelength phenomena (local modelling). Most data show correlation in space as well as in frequency, and the kernel functions with their simultaneous space and frequency localization allow for the efficient detection and approximation of essential features in the data by only using fractions of the original information (decorrelation). Using kernels at different scales (*multiscale modelling*), the corresponding approximation techniques can be constructed as to be suitable for the particular data situation.

In this article we are concerned with *wavelet techniques* for the parametrization of the Mie-representation, i.e. methods based on certain classes of kernel functions, the so-called *scaling functions and wavelets*. Suitably constructed wavelets admit a basis property in certain function spaces the elements of which – the data functions – admit a series representation in terms of a structured sequence of kernels at different positions and at different scales (*multiscale approximation*). It is thus possible to break up complicated functions like the geomagnetic field, electric current densities or geopotentials, into different pieces and to study these pieces separately. Consequently, the efficiency of wavelets lies in the fact that only a few wavelet coefficients are needed in areas where the data is smooth, and in regions where the data exhibits more complicated features higher resolution approximations can be derived by 'zooming-in' with more and more wavelets of higher scales and consequential stronger space-localization.

The outline of the paper is as follows: In Chapter 2 the fundamentals, like necessary notation as well as representation theorems for vector fields (Helmholtz-decomposition theorem for spherical and the Mie-representation theorem for solenoidal vector fields) are presented. In Chapter 3 it is recapitulated how the Mie-representation can be applied in satellite magnetometry in order to interpret different source terms and their geomagnetic effects. In Chapter 4 scalar and vectorial scaling functions and wavelets for the analysis of square-integrable scalar and vectorial spherical functions are introduced. In Chapter 5 the Helmholtz-decomposition theorem is utilized to combine the wavelet techniques and the Mie-representation of the geomagnetic field to what is called the *wavelet-Mie-representation*. The resulting method of data analysis is illustrated in Chapter 6 where the wavelet-Mie-representation is used to calculate radial ionospheric current distributions from the toroidal geomagnetic contributions extracted from MAGSAT and CHAMP vectorial data sets.

2 Fundamentals

2.1 Notation and Preliminaries

In order to avoid notational complications we will, unless stated otherwise, use the following scheme: Scalar fields will be denoted by capital roman letters (F, G, etc.) while vector fields are symbolized by lower-case roman letters (f, g, etc.).

A sphere of radius R centered in the origin, i.e. the set $\{x \in \mathbb{R}^3 : |x| = R\}$ will be denoted by Ω_R. In particular, $\Omega (= \Omega_1)$ is the unit sphere in $\mathbb{R}^3$. A spherical shell with inner radius R_1 and outer radius R_2 is given by $\Omega_{(R_1,R_2)} = \{x \in \mathbb{R}^3 : R_1 \leq |x| \leq R_2\}$. Any element $x \in \mathbb{R}^3$ with $|x| \neq 0$ may be written in the form $x = r\xi$, where $r = |x|$ and $\xi \in \Omega$, $\xi = (\xi_1, \xi_2, \xi_3)^T$ is the uniquely determined directional unit vector of x. Using this separation the gradient ∇ in $\mathbb{R}^3$ reads

$$\nabla_x = \xi \frac{\partial}{\partial r} + \frac{1}{r} \nabla^*_\xi, \tag{1}$$

where the horizontal part ∇^* is the *surface gradient* on the unit sphere Ω. Moreover, the Laplace operator $\Delta = \nabla \cdot \nabla$ in $\mathbb{R}^3$ has the representation

$$\Delta_x = \left(\frac{\partial}{\partial r} \right)^2 + \frac{2}{r} \frac{\partial}{\partial r} + \frac{1}{r^2} \Delta^*_\xi, \tag{2}$$

where Δ^* is the *Beltrami operator* on the unit sphere Ω. The *surface curl gradient* L^* on Ω can be calculated from ∇^* by the relation $L^*_\xi = \xi \wedge \nabla^*_\xi$, $\xi \in \Omega$ (where $'\wedge'$ denotes the usual cross product).

A function is said to be of class $\mathcal{C}^{(k)}(\Omega_R)$, $0 \leq k < \infty$, if it possesses k continuous derivatives on Ω_R. The set $c^{(k)}(\Omega_R)$, $0 \leq k < \infty$, denotes the space of k-times continuously differentiable vector fields on Ω_R. The Hilbert spaces of measurable, square-integrable scalar and vector fields on the sphere Ω_R are denoted by $\mathcal{L}^2(\Omega_R)$ and $l^2(\Omega_R)$, respectively. Let $H_n : \mathbb{R}^3 \to \mathbb{R}$ be a homogeneous harmonic polynomial of degree n, then the restriction $Y_n = H_n|_\Omega$ is called a (scalar) spherical harmonic of degree n. The space of all spherical harmonics of degree n is of dimension $2n+1$. Spherical harmonics of different degrees are orthogonal in the sense of the $\mathcal{L}^2(\Omega)$-inner product

$$(Y_n, Y_m)_{\mathcal{L}^2(\Omega)} = \int_\Omega Y_n(\xi) Y_m(\xi) d\omega(\xi) = 0, \quad n \neq m.$$

Throughout the remainder of this work, we denote by $\{Y_{n,k}\}$, $n = 0, 1, \ldots,\ k = 1, \ldots 2n+1$ a complete orthonormal system in the Hilbert space $\mathcal{L}^2(\Omega)$. It is obvious that $\left\{Y^{R_1}_{n,k}\right\}$, $n = 0, 1, \ldots,\ k = 1, \ldots 2n+1$ with $Y^{R_1}_{n,k} = 1/R_1 Y_{n,k}$ denotes an $\mathcal{L}^2(\Omega_{R_1})$-orthonormal system. Let $F \in \mathcal{C}^{(0_i)}(\Omega)$, then the operators $o^{(i)}_\xi : \mathcal{C}^{(0_i)}(\Omega) \to c(\Omega)$ are given by

$$\begin{aligned} o^{(1)}_\xi F(\xi) &= \xi F(\xi), \quad \xi \in \Omega, \\ o^{(2)}_\xi F(\xi) &= \nabla^*_\xi F(\xi), \quad \xi \in \Omega, \\ o^{(3)}_\xi F(\xi) &= L^*_\xi F(\xi), \quad \xi \in \Omega, \end{aligned} \tag{3}$$

where 0_i is an abbreviation given by $0_1 = 0$ and $0_i = 1$ for $i \in \{2,3\}$. Clearly, $o_\xi^{(1)} F(\xi)$ is a radial field. From the definitions of the operators ∇^* and L^* it is easy to see that $o_\xi^{(2)} F(\xi)$ and $o_\xi^{(3)} F(\xi)$ are purely tangential. Furthermore $o_\xi^{(2)} F(\xi)$ is curl-free, whereas $o_\xi^{(3)} F(\xi)$ is divergence free, which is clear from $\nabla_\xi^* F(\xi)$ being a gradient- and $L_\xi^* F(\xi)$ being a curl-field. Additionally it is not difficult to see that

$$o_\xi^{(i)} F(\xi) \cdot o_\xi^{(j)} F(\xi) = 0, \text{ for all } i \neq j \quad i,j \in \{1,2,3\}\,. \tag{4}$$

Using a complete system of scalar spherical harmonics we are able to introduce a complete orthonormal set $\{y_{n,k}^{(i)}\}$ of vector spherical harmonics in $l^2(\Omega)$ (e.g. [15]):

$$y_{n,k}^{(i)} = (\mu_n^{(i)})^{-1/2} o^{(i)} Y_{n,k}, \tag{5}$$

$i = 1,2,3$, $n = 0_i, 0_i + 1, \ldots$, $k = 1, \ldots, 2n+1$, where the normalization factor is chosen to be

$$\mu_n^{(i)} = \begin{cases} 1 & \text{if} \quad i = 1 \\ n(n+1) & \text{if} \quad i = 2,3. \end{cases} \tag{6}$$

2.2 Helmholtz-Decomposition and Mie-Representation

The waveletMie-representations are based on two main results for the decomposition of vector fields: The Helmholtz-decomposition of spherical vector fields and the Mie-representation of solenoidal vector fields. We start with the *Helmholtz decomposition theorem:* (cf. [15])

Theorem 2.1
Let $f \in c^{(1)}(\Omega)$. Then there exist uniquely determined scalar functions $F_1 \in \mathcal{C}^{(1)}(\Omega)$ and $F_2, F_3 \in \mathcal{C}^{(2)}(\Omega)$ satisfying

$$\int_\Omega F_i(\xi) d\omega(\xi) = 0, \quad i = 2,3 \tag{7}$$

such that

$$f = \sum_{i=1}^{3} o^{(i)} F_i. \tag{8}$$

It should be mentioned that F_1 is just the radial projection of f, while representations for the Helmholtz scalars F_2 and F_3 are available in terms of the Green's function with respect to the Beltrami operator (cf. [15]). Note that the above theorem is also valid for vector fields on Ω_R, since they are isomorphic to those on Ω.

Apart from the Helmholtz representation which has been presented above, we will make use of the so-called Mie representation for solenoidal vector fields. A vector field f on an open subset $\mathcal{U} \subset \mathbb{R}^3$ is called solenoidal if and only if the integral $\int_S f(x) \cdot \nu(x) d\omega(x)$ vanishes for every closed surface S lying entirely in U (ν denotes the outward normal of S). Every such solenoidal vector field admits a representation in terms of two uniquely defined scalar functions by means of the *Mie representation theorem* (e.g. [1, 2, 18, 32]):

Theorem 2.2
Let $0 < R_1 < R_2$ and let $f : \Omega_{(R_1,R_2)} \to \mathbb{R}^3$ be a solenoidal vector field in the spherical shell $\Omega_{(R_1,R_2)}$. Then there exist unique scalar functions $P_f, Q_f : \Omega_{(R_1,R_2)} \to \mathbb{R}$, such that

(1) $\int\limits_{\Omega_r} P_f(x) d\omega_r(x) = \int\limits_{\Omega_r} Q_f(x) d\omega_r(x) = 0,$

(2) $f = \nabla \wedge LP_f + LQ_f,$

for all $r \in (R_1, R_2)$ with the operator L given by $L_x = x \wedge \nabla_x$.

Vector fields of the form $\nabla \wedge LP_f$ are called poloidal while vector fields of the form LQ_f are denoted toroidal. For the sake of completeness we present the following theorem (cf. [2]).

Theorem 2.3
Let $0 < R_1 < R_2$ and let $f : \Omega_{(R_1,R_2)} \to \mathbb{R}^3$ be a solenoidal vector field in the spherical shell $\Omega_{(R_1,R_2)}$. Then there exist a unique poloidal field p as well as a unique toroidal field t such that

$$f = p + t, \tag{9}$$

in $\Omega_{(R_1,R_2)}$.

For our further considerations it is important that, for each $x = r\xi$ with $R_1 < r < R_2$ and $\xi \in \Omega$ the Mie representation $f = \nabla \wedge LP_f + LQ_f$ can be rewritten as

$$f(r\xi) = \xi \frac{\Delta_\xi^* P_f(r\xi)}{r} - \nabla_\xi^* \frac{\partial_r r P_f(r\xi)}{r} + L_\xi^* Q_f(r\xi) \tag{10}$$

(cf. e.g. [1, 2, 25, 29]), where we have used the abbreviation $\partial_r = \partial/\partial r$. (Actually, as regards the second term, it is mathematically correct to write

$$\left(\frac{\partial}{\partial \tilde{r}} \tilde{r} P_f(\tilde{r}\xi) \right) |_{\tilde{r}=r}.$$

We avoid this awkward notation, however, and stick to the easy nomenclature.) Note that Equation (10) is the Helmholtz-decomposition of the Mie-representation of f and links the previously defined vector spherical harmonics to the Mie-representation of vector fields.

Finally, we mention a last result which is concerned with the curl of a Mie representation:

Corollary 2.4
Let $f, g : \Omega_{(R_1,R_2)} \to \mathbb{R}^3$ be two solenoidal vector fields with representations

$$\begin{aligned} f &= \nabla \wedge LP_f + LQ_f, \\ g &= \nabla \wedge LP_g + LQ_g, \end{aligned}$$

and which are connected via $\nabla \wedge f = \lambda g$, $\lambda \in \mathbb{R} \setminus \{0\}$. *Then the Mie scalars are related via*

$$\begin{aligned} P_g &= \frac{1}{\lambda} Q_f, \\ Q_g &= -\frac{1}{\lambda} \Delta P_f. \end{aligned}$$

This shows us that the curl of a poloidal field is a toroidal field, and vice versa.

3 The (Geo)Magnetic Field in Mie-Representation

If we assume the typical length and time scales of the magnetic field b and the electric current densities j to be such that retarding effects (and displacement currents) are negligible, then we can consider the quasi-static approximation of Maxwell's equations, the Pre-Maxwell equations, to be valid:

$$\begin{aligned} \nabla \cdot b &= 0, \\ \nabla \wedge b &= \mu_0 j, \end{aligned}$$

where μ_0 is the vacuum permeability. Since the magnetic field is divergence free everywhere, it can be split up into a poloidal and a toroidal part (see Theorem 2.2):

$$b = b_{pol} + b_{tor} = \nabla \wedge L P_b + L Q_b. \tag{11}$$

The quasi-static approximation being true is equivalent to the current densities being divergence free everywhere. Consequently the electric currents also admit a Mie-representation:

$$j = j_{pol} + j_{tor} = \nabla \wedge L P_j + L Q_j. \tag{12}$$

According to Corollary 2.4 the Mie scalars of the magnetic field and the electric currents are related via:

$$P_j = \frac{1}{\mu_0} Q_b, \tag{13}$$

$$Q_j = -\frac{1}{\mu_0} \Delta P_b. \tag{14}$$

Using (10) we can, for each $x = r\xi$ with $r \neq 0$ and $\xi \in \Omega$, rewrite Equations (11) and (12) as

$$b = \xi \frac{\Delta_\xi^* P_b}{r} - \nabla_\xi^* \frac{\partial_r r P_b}{r} + L_\xi^* Q_b \tag{15}$$

and

$$j = \xi \frac{\Delta_\xi^* P_j}{r} - \nabla_\xi^* \frac{\partial_r r P_j}{r} + L_\xi^* Q_j. \tag{16}$$

The first two terms in Equations (15) and (16) can be interpreted as the restriction of the poloidal magnetic field b_{pol} and the poloidal currents j_{pol} to the sphere Ω_r, respectively. The last terms represent the toroidal field b_{tor} and currents j_{tor} on Ω_r. These equations will serve as a starting point for the wavelet-Mie-representations in Section 5.

Following Backus [1], Engels and Olsen [11] and Maus [25], we assume either the geomagnetic field b or the electric current distributions j to be sampled within a spherical shell $\Omega_{(R_1,R_2)}$, $0 < R_1 < R_2 < \infty$. This assumption takes into account elliptical satellite orbits as well as the decrease in altitude with the lifetime of the satellite. The geomagnetic field within the shell $\Omega_{(R_1,R_2)}$ consists of four different parts (cf. [29]), i.e.

$$b = b_{pol}^{int} + b_{pol}^{ext} + b_{pol}^{sh} + b_{tor}. \tag{17}$$

b_{pol}^{int} denotes the poloidal magnetic field due internal toroidal currents in the region with $r < R_1$. b_{pol}^{ext} is the poloidal part caused by external toroidal current densities in the region with $r > R_2$, and b_{pol}^{sh} is the poloidal magnetic field due to the toroidal electric currents within $\Omega_{(R_1,R_2)}$. Finally, b_{tor} is the toroidal part of b generated by poloidal currents in $\Omega_{(R_1,R_2)}$. If there are no currents in the shell $\Omega_{(R_1,R_2)}$, then $b_{pol}^{sh} = b_{tor} = 0$ and b can be represented as the gradient field of a scalar harmonic potential or by means of the Mie representation equivalently. If only the toroidal currents vanish within the shell, then $b_{pol}^{sh} = 0$, and the magnetic field within the shell can be represented by

$$b = b_{pol}^{int} + b_{pol}^{ext} + b_{tor}. \tag{18}$$

The situation changes if the toroidal currents within the shell $\Omega_{(R_1,R_2)}$ do not vanish. Let us suppose that the radii of the shell satisfy

$$R_2 - R_1 << \frac{R_2 + R_1}{2}, \tag{19}$$

i.e. the thickness of the shell is small compared to the mean radius. Such a shell is called a *thin shell*. As pointed out by Backus [1] and Olsen [29], even for non-vanishing (toroidal) current densities in the shell, the magnetic field within a thin shell can (approximately) be represented by (18), i.e. the poloidal field b_{pol}^{sh} tends to zero in thin shells while the toroidal part b_{tor} remains finite. Actually, for thin shells, it holds that $b_{pol}^{sh} \to 0$ as $(R_2 - R_1)/H \to 0$, where H is a reference length characterizing the vertical scale of the current density (e.g. [1, 29]). In more detail, if in a thin shell,

$$R_2 - R_1 << H \simeq \frac{R_2 + R_1}{2}, \tag{20}$$

i.e. the current density changes significantly on vertical scales that can be compared to the mean radius and that are much larger than the thickness of the shell, then the thin shell approximation (18) is surely valid. If, in a thin shell,

$$R_2 - R_1 \simeq H << \frac{R_2 + R_1}{2}, \tag{21}$$

i.e. the currents change significantly on vertical length scales that are small compared to the mean radius but that can be compared to the thickness of the shell, then the thin shell approximation can as well fail. For more details the interested reader is directed to [1]. In what follows we assume the thin shell approximation to be valid (which is a reasonable assumption for the examples presented in Section 6, see e.g. [29] and [25]).

At this point, there remains the question of how to numerically obtain - in terms of suitable trial functions- the Mie-representation of a given set of vectorial data. As we

have already mentioned, the global support of the spherical harmonics limits the practicability of spherical harmonic parametrizations since most of the relevant ionospheric currents vary rapidly with latitude and longitude and/or are confined to certain regions. Consequently, it seems reasonable to find a field parametrization in terms of functions that take efficient account of the specific concentration of the current densities in space. In [4] we have already presented first methods to deal with the Mie representation in terms of space localizing trial functions, so-called spherical vectorial wavelets, which are able to reflect various levels of space localization (see also [3]). The techniques developed in Section 5 are generalizations and enhancements of this approach. For a complete and comprehensive description the interested reader is directed to the thesis [24].

4 Scaling Functions and Wavelets in $\mathcal{L}^2(\Omega)$ and $l^2(\Omega)$

As far as this article is concerned, it suffices to introduce scaling functions and wavelets for the spaces of square-integrable scalar and vector fields on the unit sphere, i.e. $\mathcal{L}^2(\Omega)$ and $l^2(\Omega)$. This theory is well known since, starting from classical wavelet theory (see e.g. [7] and [6] for an overview), the concept of multiresolution has been adapted to spherical geometries for scalar fields by e.g. Freeden and Windheuser [16, 17] and, for vector fields, by Bayer et al. [3] and Freeden et al. [15], for example. We therefore just repeat some results which are useful for our further considerations:
A real sequence $\{(\Phi_J)^\wedge(n)\}$, $J \in \mathbb{Z}$, $n \in \mathbb{N}_0$ is called a generator (or symbol) of an $\mathcal{L}^2(\Omega)$-scaling function if it satisfies:

(i) $\sum\limits_{n=0}^{\infty} \left((\Phi_J)^\wedge(n)\right)^2 < \infty$,

(ii) $\sum\limits_{n=0}^{\infty} \left((\Phi_J)^\wedge(n) Y_{n,k}(\xi)\right)^2 < \infty$, for all $\xi \in \Omega$,

(iii) $\lim\limits_{J\to\infty} \left((\Phi_J)^\wedge(n)\right)^2 = 1$, $n \in \mathbb{N}$,

(iv) $\left((\Phi_J)^\wedge(n)\right)^2 \geq \left((\Phi_{J-1})^\wedge(n)\right)^2$

(v) $\lim\limits_{J\to-\infty} \left((\Phi_J)^\wedge(n)\right)^2 = 0$,

(vi) $\left((\Phi_J)^\wedge(0)\right)^2 = 1$, $J \in \mathbb{Z}$.

The corresponding family $\{\Phi_J\}$ of kernels given by

$$\Phi_J(\xi,\eta) = \sum_{n=0}^{\infty} \sum_{k=1}^{2n+1} (\Phi_J)^\wedge(n) Y_{n,k}(\xi) Y_{n,k}(\eta), \tag{22}$$

$\xi, \eta \in \Omega$ is called $\mathcal{L}^2(\Omega)$-scaling function. The real sequence $\{(\Psi_J)^\wedge(n)\}$, $J \in \mathbb{Z}$, $n \in \mathbb{N}_0$ defined via the refinement equation

$$(\Psi_J)^\wedge(n) = \left(((\Phi_{J+1})^\wedge(n))^2 - ((\Phi_J)^\wedge(n))^2\right)^{\frac{1}{2}}, \tag{23}$$

is called the generator (or symbol) of the $\mathcal{L}^2(\Omega)$-wavelet $\{\Psi_J\}$ given as

$$\Psi_J(\xi, \eta) = \sum_{n=0}^{\infty} \sum_{k=1}^{2n+1} (\Psi_J)^\wedge(n) Y_{n,k}(\xi) Y_{n,k}(\eta), \tag{24}$$

$\xi, \eta \in \Omega$.

Let, for $i \in \{1, 2, 3\}$, the real sequence $\left\{\left(\varphi_J^{(i)}\right)^\wedge(n)\right\}$, $J \in \mathbb{Z}$, $n \in \mathbb{N}_{0_i}$ be generators of $\mathcal{L}^2(\Omega)$-scaling functions, then the vectorial kernels

$$\varphi_J^{(i)}(\xi, \eta) = \sum_{n=0_i}^{\infty} \sum_{k=1}^{2n+1} (\varphi_J^{(i)})^\wedge(n) Y_{n,k}(\xi) y_{n,k}^{(i)}(\eta), \tag{25}$$

are called $l^2(\Omega)$-scaling functions of type i. The $l^2(\Omega)$-wavelets of type i are given by

$$\psi_J^{(i)}(\xi, \eta) = \sum_{n=0_i}^{\infty} \sum_{k=1}^{2n+1} (\psi_J^{(i)})^\wedge(n) Y_{n,k}(\xi) y_{n,k}^{(i)}(\eta), \tag{26}$$

with generators $\left\{\left(\psi_J^{(i)}\right)^\wedge(n)\right\}$ satisfying the refinement equation

$$(\psi_J^{(i)})^\wedge(n) = \left(\left((\varphi_{J+1}^{(i)})^\wedge(n)\right)^2 - \left((\varphi_J^{(i)})^\wedge(n)\right)^2\right)^{\frac{1}{2}}. \tag{27}$$

With these definitions at hand, we can find approximations of $\mathcal{L}^2(\Omega)$ and $l^2(\Omega)$ functions in terms of the respective scaling functions and wavelets (e.g. [16]):

Theorem 4.1
Let the families $\{\Phi_J\}$, $\{\Psi_J\}$ be $\mathcal{L}^2$-scaling functions and wavelets. For any $F \in \mathcal{L}^2(\Omega)$ it holds that

$$F = \Phi_{J'} * \Phi_{J'} * F + \sum_{J=J'}^{\infty} \Psi_J * \Psi_J * F \tag{28}$$

$$= \Phi_0 * \Phi_0 * F + \sum_{J=0}^{\infty} \Psi_J * \Psi_J * F, \tag{29}$$

where the convolution operator '$*$' for scalar kernels and functions is defined by

$$K * F = \int_\Omega K(\cdot, \eta) F(\eta)\, d\omega(\eta). \tag{30}$$

In the case of vector fields $f \in l^2(\Omega)$ it is possible to show the following (cf. [3]):

Theorem 4.2
Let the families $\{\varphi_J^{(i)}\}$, $\{\psi_J^{(i)}\}$, *be vectorial scaling functions and wavelets. Then, for* $f \in l^2(\Omega)$,

$$f = \sum_{i=1}^{3} \varphi_{J'}^{(i)} \star \varphi_{J'}^{(i)} * f + \sum_{J=J'}^{\infty} \sum_{i=1}^{3} \psi_J^{(i)} \star \psi_J^{(i)} * f \tag{31}$$

$$= \sum_{i=1}^{3} \varphi_0^{(i)} \star \varphi_0^{(i)} * f + \sum_{J=0}^{\infty} \sum_{i=1}^{3} \psi_J^{(i)} \star \psi_J^{(i)} * f \tag{32}$$

where the convolution '$*$*' of a vectorial kernel against a vector field is given as*

$$k * f = \int_\Omega k(\cdot, \eta) \cdot f(\eta)\, d\omega(\eta), \tag{33}$$

and the convolution '$\star$*' of a vectorial kernel against a scalar field is*

$$k \star F = \int_\Omega k(\eta, \cdot) F(\eta)\, d\omega(\eta). \tag{34}$$

The representations of square-integrable scalar and vectorial functions in terms of scaling functions and wavelets build one of the fundamentals for our considerations in the next section. It is noteworthy that the vectorial wavelets are defined in correspondence to the vector spherical harmonics in Section 2.1 and can therefore be linked to the Mie-representation via Equations (10), (15) and (16), which is the task of the next section.

It should be remarked that, in the case of F being one of the Mie-scalars, the first term in (29) vanishes, since the Mie-scalars have vanishing zeroth order moment. A similar argument holds true for the case of f being the magnetic field or the electric current density, i.e. since both are of zero divergence the first term in (32) vanishes.

Before we go on, we mention some properties of the above kernel functions (scaling functions and wavelets) which are important from a numerical point of view. Let K and $k^{(i)}$ be either scalar scaling functions or wavelets, or vectorial scaling functions or wavelets, respectively. Using the addition theorem for spherical harmonics each scalar kernel K admits the following representation:

$$K(\xi, \eta) = \sum_{n=0}^{\infty} \sum_{k=1}^{2n+1} (K)^\wedge(n) Y_{n,k}(\xi) Y_{n,k}(\eta) \tag{35}$$

$$= \sum_{n=0}^{\infty} (K)^\wedge(n) \frac{2n+1}{4\pi} P_n(\xi \cdot \eta), \tag{36}$$

where P_n is the Legendre polynomial of degree n. For the evaluation of such series of Legendre polynomials there exist fast and stable recursive algorithms (e.g. [8]).

In the case of vectorial kernels, the situation is only slightly more complicated. From the definition of the vector spherical harmonics and the vectorial kernel functions (see

Equations (5), (25) and (26)) we see that

$$k^{(i)}(\xi,\eta) = \sum_{n=0_i}^{\infty}\sum_{k=1}^{2n+1}(k^{(i)})^{\wedge}(n)\,Y_{n,k}(\eta)\,\left(\mu_n^{(i)}\right)^{-\frac{1}{2}}\,o_\xi^{(i)}Y_{n,k}(\xi) \tag{37}$$

$$= o_\xi^{(i)}\sum_{n=0_i}^{\infty}\sum_{k=1}^{2n+1}(k^{(i)})^{\wedge}(n)\,Y_{n,k}(\eta)\,\left(\mu_n^{(i)}\right)^{-\frac{1}{2}}\,Y_{n,k}(\xi) \tag{38}$$

$$= o_\xi^{(i)}\sum_{n=0_i}^{\infty}\frac{2n+1}{4\pi}\,(k^{(i)})^{\wedge}(n)\,\left(\mu_n^{(i)}\right)^{-\frac{1}{2}}\,P_n(\xi\cdot\eta). \tag{39}$$

For $\eta\in\Omega$ fixed, the Legendre polynomials are isotropic functions on the unit sphere and the $o^{(i)}$ can be applied. This results in

$$o_\xi^{(1)}P_n(\xi\cdot\eta) = \xi P_n(\xi\cdot\eta), \tag{40}$$

$$o_\xi^{(2)}P_n(\xi\cdot\eta) = (\eta-(\xi\cdot\eta)\,\xi)\;P_n'(\xi\cdot\eta), \tag{41}$$

$$o_\xi^{(3)}P_n(\xi\cdot\eta) = (\xi\wedge\eta)\,P_n'(\xi\cdot\eta)\,. \tag{42}$$

Using this, the kernels in Equation (39) admit the following representation:

$$k^{(1)}(\xi,\eta) = \xi\sum_{n=0}^{\infty}\frac{2n+1}{4\pi}\,(k^{(i)})^{\wedge}(n)\,\left(\mu_n^{(i)}\right)^{-\frac{1}{2}}\,P_n(\xi\cdot\eta), \tag{43}$$

$$k^{(2)}(\xi,\eta) = (\eta-(\xi\cdot\eta)\,\xi)\sum_{n=1}^{\infty}\frac{2n+1}{4\pi}\,(k^{(i)})^{\wedge}(n)\,\left(\mu_n^{(i)}\right)^{-\frac{1}{2}}\,P_n'(\xi\cdot\eta), \tag{44}$$

$$k^{(3)}(\xi,\eta) = (\xi\wedge\eta)\sum_{n=1}^{\infty}\frac{2n+1}{4\pi}\,(k^{(i)})^{\wedge}(n)\,\left(\mu_n^{(i)}\right)^{-\frac{1}{2}}\,P_n'(\xi\cdot\eta), \tag{45}$$

such that the fast and stable one-dimensional recursive algorithms can as well be used for calculating the vectorial kernels. It should be noted that, if the kernel functions are non-bandlimited (non-degenerate), the sums in the above equations need to be truncated if no analytic representation for the kernels are known.

For later use we present, as a certain choice of possible kernels, the vectorial cubic polynomial wavelets which can be derived by using a generator of the form

$$\varphi_0^{(i)}(x) = \begin{cases} (1-x)^2(1+2x) & , \quad x\in[0,1) \\ 0 & , \quad x\in[1,\infty). \end{cases}$$

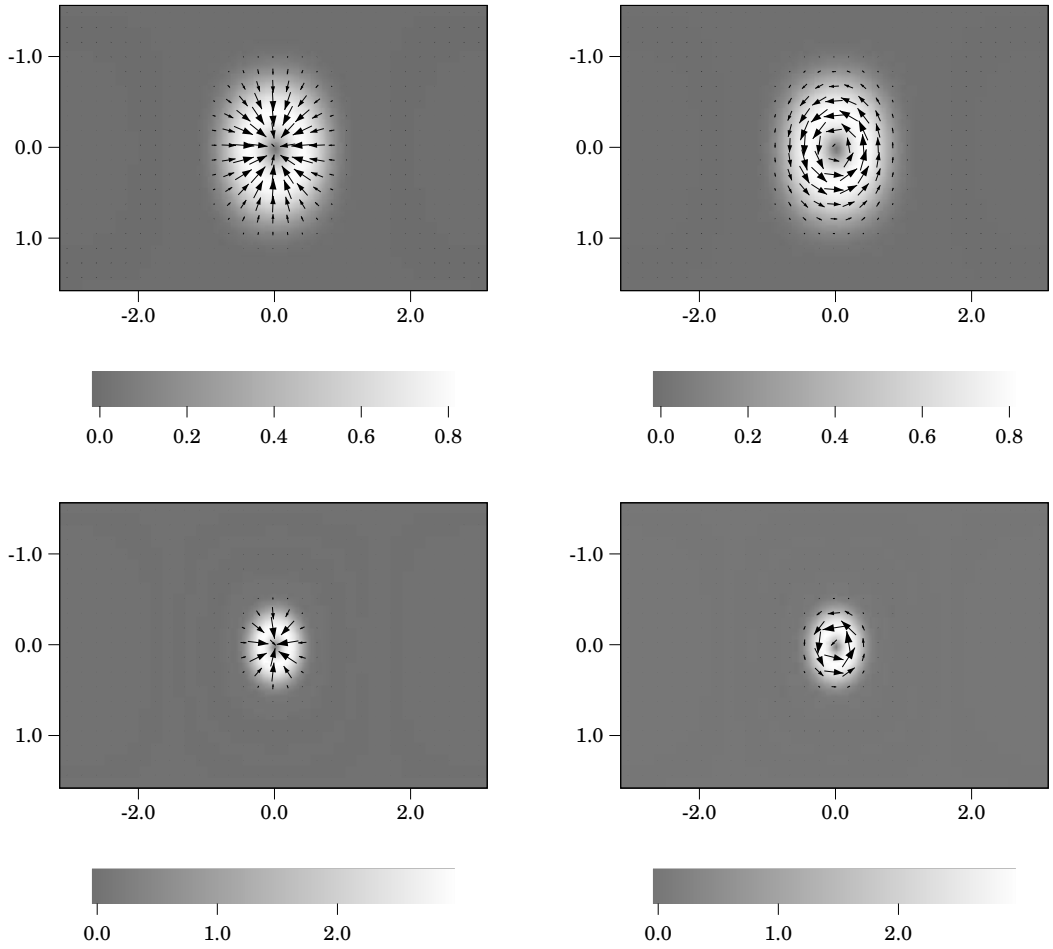

Figure 1: Cubic polynomial wavelets in the longitude-latitude-plane. Arrows indicate direction and color indicates magnitude. Top: Curl-free ($i = 2$, left) and divergence-free ($i = 3$, right) CuP wavelets at scale $j = 2$. Bottom: Curl-free ($i = 2$, left) and divergence-free ($i = 3$, right) CuP wavelets at scale $j = 3$.

Figure 1 provides illustrations of tangential CuP vectorial wavelets in the longitude-latitude-plane. Note that the significant support of the wavelets decreases with increasing scale, a feature typical for wavelets. It is this property that, via the wavelet-Mie-representation, allows for the analysis and modelling of spatially confined structures in the geomagnetic field and the corresponding current distributions.

5 Wavelet-Mie-Parametrizations

In what follows we restrict ourselves to the wavelet parametrization of toroidal magnetic fields and the corresponding poloidal electric current densities in the spherical shell $\Omega_{(R_1,R_2)}$. This case is sufficient for the applications presented in Section 6. For details on the wavelet parametrization of poloidal magnetic fields the reader may consult our treatise in [24]. This approach, however, requires the introduction of inner and outer harmonic wavelets (e.g. [13]) which is beyond the scope of this article.

Starting point for our considerations is a separation of variables for the toroidal field scalar Q_b, i.e. we assume that

$$Q_b(r\xi) = Q_{b,1}(r)Q_{b,2}(\xi) \text{ in } \Omega_{(R_1,R_2)}. \tag{46}$$

Relation (13) suggests to proceed likewise in the case of the scalar P_j for the poloidal currents, hence we suppose that

$$\begin{aligned} P_j(r\xi) &= P_{j,1}(r)P_{j,2}(\xi) &(47)\\ &= \frac{1}{\mu_0}Q_{b,1}(r)Q_{b,2}(\xi) \text{ in } \Omega_{(R_1,R_2)}. &(48)\end{aligned}$$

The results of Section 4 yield that the angular parts $Q_{b,2}$ and $P_{j,2}$ can be expanded in terms of scalar spherical $\mathcal{L}^2(\Omega)$-wavelets $\{\Psi_J\}$, i.e.

$$\begin{aligned} Q_{b,2} &= \sum_{J=0}^{\infty} \Psi_J * \Psi_J * Q_{b,2} &(49)\\ P_{j,2} &= \sum_{J=0}^{\infty} \Psi_J * \Psi_J * P_{j,2}. &(50)\end{aligned}$$

Combining this with (11)-(12) and (15)-(16) we can come up with the following representations for the toroidal magnetic field and the corresponding poloidal current density:

Theorem 5.1
Let, for $J \in \mathbb{Z}$, $\{\Psi_J\}$ be an $\mathcal{L}^2(\Omega)$-wavelet. Under the assumptions above, the toroidal magnetic field in $\Omega_{(R_1,R_2)}$ can be represented via

$$\begin{aligned} b_{tor}(r\cdot) = \quad & Q_{b,1}(r)\left(\bar{\varphi}^{(3)}_{J'} \star \Phi_{J'} * Q_{b,2} + \sum_{J=J'}^{\infty} \bar{\psi}^{(3)}_J \star \Psi_J * Q_{b,2}\right) &(51)\\ = \quad & Q_{b,1}(r)\left(\bar{\varphi}^{(3)}_0 \star \Phi_0 * Q_{b,2} + \sum_{J=0}^{\infty} \bar{\psi}^{(3)}_J \star \Psi_J * Q_{b,2}\right) &(52)\\ = \quad & Q_{b,1}(r)\sum_{J=0}^{\infty} \bar{\psi}^{(3)}_J \star \Psi_J * Q_{b,2}, &(53)\end{aligned}$$

where the vectorial kernels $\bar{\varphi}^{(3)}_J$ and $\bar{\psi}^{(3)}_J$ are given via $\bar{\varphi}^{(3)}_J(\xi,\eta) = L^*_\xi \Phi_J(\xi,\eta)$ and $\bar{\psi}^{(3)}_J(\xi,\eta) = L^*_\xi \Psi_J(\xi,\eta)$.

The corresponding poloidal current density in $\Omega_{(R_1,R_2)}$ is given by

$$\begin{aligned}
\mu_0 j_{pol}(r\cdot) &= \frac{1}{r}Q_{b,1}(r)\left(\tilde{\varphi}^{(1)}_{J'} \star \Phi_{J'} * Q_{b,2} + \sum_{J=J'}^{\infty} \tilde{\psi}^{(1)}_{J} \star \Psi_J * Q_{b,2}\right) + && (54)\\
&+ (\partial_r + \frac{1}{r})Q_{b,1}(r)\left(\hat{\varphi}^{(2)}_{J'} \star \Phi_{J'} * Q_{b,2} + \sum_{J=J'}^{\infty} \hat{\psi}^{(2)}_{J} \star \Psi_J * Q_{b,2}\right) && (55)\\
&= \frac{1}{r}Q_{b,1}(r)\left(\tilde{\varphi}^{(1)}_{0} \star \Phi_0 * Q_{b,2} + \sum_{J=0}^{\infty} \tilde{\psi}^{(1)}_{J} \star \Psi_J * Q_{b,2}\right) + && (56)\\
&+ (\partial_r + \frac{1}{r})Q_{b,1}(r)\left(\hat{\varphi}^{(2)}_{0} \star \Phi_0 * Q_{b,2} + \sum_{J=0}^{\infty} \hat{\psi}^{(2)}_{J} \star \Psi_J * Q_{b,2}\right) && (57)\\
&= \frac{1}{r}Q_{b,1}(r)\sum_{J=0}^{\infty} \tilde{\psi}^{(1)}_{J} \star \Psi_J * Q_{b,2} + && (58)\\
&+ (\partial_r Q_{b,1}(r) + \frac{1}{r}Q_{b,1}(r))\sum_{J=0}^{\infty} \hat{\psi}^{(2)}_{J} \star \Psi_J * Q_{b,2}, && (59)
\end{aligned}$$

where the kernel functions $\tilde{\varphi}^{(1)}_J$ and $\hat{\varphi}^{(2)}_J$ as well as $\tilde{\psi}^{(1)}_J$ and $\hat{\psi}^{(2)}_J$ are defined to be $\tilde{\varphi}^{(1)}_J(\xi,\eta) = \xi\Delta^*_\xi\Phi_J(\xi,\eta)$ and $\hat{\varphi}^{(2)}_J(\xi,\eta) = -\nabla^*_\xi\Phi_J(\xi,\eta)$, as well as $\tilde{\psi}^{(1)}_J(\xi,\eta) = \xi\Delta^*_\xi\Psi_J(\xi,\eta)$ and $\hat{\psi}^{(2)}_J(\xi,\eta) = -\nabla^*_\xi\Psi_J(\xi,\eta)$.

Proof:
Equation (51) follows from (11), (15) and (49). Theorems 4.1 and 4.2 lead to (52). The fact that the magnetic field is of zero divergence everywhere implies - via the Gauss theorem - that the magnetic field has vanishing zeroth order moment (i.e. the magnetic field is solenoidal), which means that

$$Q_{b,1}(r)\left(\bar{\varphi}^{(3)}_0 \star \Phi_0 * Q_{b,2}\right) = 0. \tag{60}$$

Equations (54) and (55) follow from (12), (16) and (50) in combination with (14). Theorems 4.1 and 4.2 then imply (56) and (57). Since in the Pre-Maxwell approximation the current density is solenoidal, too, it follows that

$$\frac{1}{r}Q_{b,1}(r)\left(\tilde{\varphi}^{(1)}_0 \star \Phi_0 * Q_{b,2}\right) = 0 \tag{61}$$

and

$$(\partial_r + \frac{1}{r})Q_{b,1}(r)\left(\hat{\varphi}^{(2)}_0 \star \Phi_0 * Q_{b,2}\right) = 0. \tag{62}$$

□

Note that all the occurring kernel functions can be calculated using the rules and results of Equations (40)-(45), as well as the fact that scalar spherical harmonics of degree n are eigenfunctions of the Beltrami operator with respect to eigenvalues $-n(n+1)$.

Theorem 5.1 presents the wavelet-Mie-representation of the toroidal magnetic field and the corresponding poloidal electric currents in the spherical shell $\Omega_{(R_1,R_2)}$. Due to the

space localization of the ansatz functions, this representation yields the possibility to use or derive different models of Q_b in different regions depending on the underlying physical effects and, of course, the data situation.

The ansatz (46) is quite simple and might fail if the radial dependency is very complex (see also the considerations in [25]). Nevertheless, assumption (46) is reasonable as long as the data situation is such that the radial behavior of the field is difficult to extract. This is arguably the case when using data from single satellite missions (see also the comments in [1], [29] and [25] concerning time-variations and single satellite missions). Nevertheless, if the data situation allows for determination of higher order radial dependencies (e.g. if data from multi-satellite missions are used, or if measurements from satellites are combined with terrestrial observations) we might expand our ansatz by adding further toroidal scalars with different radial behavior (cf. [24]).

The product ansatz for the toroidal field scalar Q_b is reflected in the corresponding toroidal magnetic field as well as in the representation of the corresponding poloidal current density. As regards the poloidal current, both its radial and its tangential parts admit a product representation, too. In more detail, let j_{rad} and j_{∇^*} be the radial and the tangential parts of j_{pol}, respectively. Then Equations (58) and (59) of Theorem 5.1 show that j_{rad} and j_{∇^*} can be represented as

$$j_{rad}(r\xi) = J_{rad,1}(r) j_{rad,2}(\xi) \tag{63}$$

and

$$j_{\nabla^*}(r\xi) = J_{\nabla^*,1}(r) j_{\nabla^*,2}(\xi), \tag{64}$$

where the scalar functions $J_{rad,1}(r)$ and $J_{\nabla^*,1}(r)$ are given via

$$\mu_0 J_{rad,1}(r) = \frac{1}{r} Q_{b,1}(r), \tag{65}$$

$$\mu_0 J_{\nabla^*,1}(r) = (\partial_r Q_{b,1}(r) + \frac{1}{r} Q_{b,1}(r)) \tag{66}$$

and the vectorial parts are

$$\mu_0 j_{rad,2} = \sum_{J=0}^{\infty} \tilde{\psi}_J^{(1)} \star \Psi_J * Q_{b,2}, \tag{67}$$

$$\mu_0 j_{\nabla^*,2} = \sum_{J=0}^{\infty} \hat{\psi}_J^{(2)} \star \Psi_J * Q_{b,2}. \tag{68}$$

Using the ansatz (46) together with (16) immediately leads us to the same results for $J_{rad,1}$ and $J_{\nabla^*,1}$ but, as regards $j_{rad,2}$ and $j_{\nabla^*,2}$, we end up with

$$\mu_0 j_{rad,2}(\xi) = \xi \Delta_\xi^* Q_{b,2}(\xi), \tag{69}$$

$$\mu_0 j_{\nabla^*,2}(\xi) = -\nabla_\xi^* Q_{b,2}(\xi), \tag{70}$$

which is independent from any parametrization of Q_b. Nevertheless, we know from Section 4) that we can expand the radial vector field $\mu_0 j_{rad,2}$ and the tangential vector field $\mu_0 j_{\nabla^*,2}$ using vectorial $l^2(\Omega)$-wavelets $\left\{\psi_J^{(i)}\right\}$ of type $i = 1$ and $i = 2$, respectively. Consequently we are led to the following alternative representation in terms of $l^2(\Omega)$-wavelets:

Corollary 5.2
Let the families $\{\varphi_J^{(i)}\}$, $\{\psi_J^{(i)}\}$, $i = 1, 2$, *be vectorial scaling functions and wavelets. The radial part* j_{rad} *and tangential part* j_{∇^*} *of the poloidal current density can be represented via*

$$\begin{aligned}
j_{rad}(r\cdot) = &\quad \varphi_{J'}^{(1)} \star \left(\varphi_{J'}^{(1)} * j_{rad}\right)(r) + \sum_{J=J'}^{\infty} \psi_J^{(1)} \star \left(\psi_J^{(1)} * j_{rad}\right)(r) && (71)\\
= &\quad \varphi_0^{(1)} \star \left(\varphi_0^{(1)} * j_{rad}\right)(r) + \sum_{J=0}^{\infty} \psi_J^{(1)} \star \left(\psi_J^{(1)} * j_{rad}\right)(r) && (72)\\
= &\quad \sum_{J=0}^{\infty} \psi_J^{(1)} \star \left(\psi_J^{(1)} * j_{rad}\right)(r) && (73)\\
= &\quad \frac{1}{r} Q_{b,1}(r) \sum_{J=0}^{\infty} \psi_J^{(1)} \star \psi_J^{(1)} * j_{rad,2} && (74)\\
= &\quad \sum_{J=0}^{\infty} \psi_J^{(1)} \star \left(\psi_J^{(1)} * j\right)(r), && (75)
\end{aligned}$$

and

$$\begin{aligned}
j_{\nabla^*}(r\cdot) = &\quad \varphi_{J'}^{(2)} \star \left(\varphi_{J'}^{(2)} * j_{rad}\right)(r) + \sum_{J=J'}^{\infty} \psi_J^{(2)} \star \left(\psi_J^{(2)} * j_{rad}\right)(r) && (76)\\
= &\quad \varphi_0^{(2)} \star \left(\varphi_0^{(2)} * j_{rad}\right)(r) + \sum_{J=0}^{\infty} \psi_J^{(2)} \star \left(\psi_J^{(2)} * j_{rad}\right)(r) && (77)\\
= &\quad \sum_{J=0}^{\infty} \psi_J^{(2)} \star \left(\psi_J^{(2)} * j_{\nabla^*}\right)(r) && (78)\\
= &\quad (\partial_r + \frac{1}{r}) Q_{b,1}(r) \sum_{J=0}^{\infty} \psi_J^{(2)} \star \psi_J^{(2)} * j_{\nabla^*,2} && (79)\\
= &\quad \sum_{J=0}^{\infty} \psi_J^{(2)} \star \left(\psi_J^{(2)} * j\right)(r). && (80)
\end{aligned}$$

Note that equations (75) and (80) are true since only the poloidal current density does contain a radial or ∇^*-contribution (see (16)). In other words, on each Ω_r with $R_1 < r < R_2$, the radial current density can be derived from expanding the total current density in terms of spherical vectorial wavelets of type $i = 1$ while the tangential part of the poloidal current density can be calculated via spherical vectorial wavelets of type $i = 2$. Equations (73)-(80) can therefore be used to determine the toroidal field scalar or, of course, the corresponding toroidal magnetic field.

A similar approach can be applied in order to determine the poloidal current density j_{pol} in $\Omega_{(R_1,R_2)}$ from the corresponding toroidal field b_{tor}. Assuming the product ansatz for Q_b and applying (15) we see that the toroidal magnetic field admits a product representation as well, i.e.

$$b_{tor}(r\xi) = B_{tor,1}(r) b_{tor,2}(\xi) \qquad (81)$$

where $b_{tor,2} = L^* Q_{b,2}$ can be expressed in terms of spherical vectorial $l^2(\Omega)$-wavelets $\left\{\psi_J^{(3)}\right\}$ of type $i = 3$ as follows

$$b_{tor,2} = \sum_{J=0}^{\infty} \psi_J^{(3)} \star \psi_J^{(3)} * b_{tor,2}. \tag{82}$$

From our previous results we know that the scalar $B_{tor,1}$ is just given by

$$B_{tor,1}(r) = Q_{b,1}(r). \tag{83}$$

Since the toroidal magnetic field b_{tor} is the only part of b that contributes a L^*-portion it is clear that

$$\begin{aligned} b_{tor}(r\cdot) &= \sum_{J=0}^{\infty} \psi_J^{(3)} \star \left(\psi_J^{(3)} * b_{tor}\right)(r) && (84)\\ &= \sum_{J=0}^{\infty} \psi_J^{(3)} \star \left(\psi_J^{(3)} * b\right)(r), && (85) \end{aligned}$$

on any sphere Ω_r with $R_1 < r < R_2$. Summarizing the above considerations we are led to

Corollary 5.3
Let the families $\{\varphi_J^{(3)}\}$, $\{\psi_J^{(3)}\}$, be vectorial scaling functions and wavelets of type 3. The toroidal magnetic field b_{tor} can be represented via

$$\begin{aligned} b_{tor}(r\cdot) &= Q_{b,1}(r)\left(\varphi_{J'}^{(3)} \star \varphi_{J'}^{(3)} * b_{tor,2} + \sum_{J=J'}^{\infty} \psi_J^{(3)} \star \psi_J^{(3)} * b_{tor,2}\right) && (86)\\ &= Q_{b,1}(r)\left(\varphi_0^{(3)} \star \varphi_0^{(3)} * b_{tor,2} + \sum_{J=0}^{\infty} \psi_J^{(3)} \star \psi_J^{(3)} * b_{tor,2}\right) && (87)\\ &= Q_{b,1}(r)\sum_{J=0}^{\infty} \psi_J^{(3)} \star \psi_J^{(3)} * b_{tor,2} && (88)\\ &= \sum_{J=0}^{\infty} \psi_J^{(3)} \star \left(\psi_J^{(3)} * b\right)(r) && (89) \end{aligned}$$

on any sphere Ω_r with $R_1 < r < R_2$.

This yields one possible way of determining the poloidal field scalar (and consequently the corresponding poloidal electric current density) from magnetic measurements in $\Omega_{(R_1,R_2)}$.

Assuming that the data are only given at constant altitude (or with negligible radial dependencies), the previous approach can be easily applied to calculate radial current densities on a sphere Ω_r, with $R_1 < r < R_2$, from measurements of the magnetic field on that very sphere. We assume that the magnetic field b is sampled on a dense grid on the sphere Ω_r. We make use of the fact that, with a suitably chosen maximum scale J_{max}, we can approximate the toroidal part b_{tor} on Ω_r via a series expansion in terms of $l^2(\Omega)$-wavelets (see Corollary 5.3):

$$b_{tor}(r\xi) \simeq \left(\sum_{J=0}^{J_{max}} \psi_J^{(3)} \star \left(\psi_J^{(3)} * b\right)(r)\right)(\xi). \tag{90}$$

Using the fact that $b_{tor}(r,\cdot) = L^* Q_b$ we immediately get an approximation for the toroidal scalar, i.e.

$$Q_b(r\xi) \simeq \left(\sum_{J=0}^{J_{max}} \tilde{\Psi}_J * \left(\psi_J^{(3)} * b \right)(r) \right)(\xi) \tag{91}$$

where the kernel $\tilde{\Psi}_J$ is given such that the relation $\psi_J^{(3)}(\eta,\xi) = L_\xi^* \tilde{\Psi}_J(\eta,\xi)$ holds true. Using (91) together with (16) we arrive at an approximation of the radial current density on Ω_r corresponding to the toroidal magnetic field there:

$$\begin{aligned} \mu_0 j_{rad}(r\xi) &= \frac{1}{r} \xi \Delta_\xi^* Q_b(r\xi) \\ &\simeq \frac{1}{r} \left(\sum_{J=0}^{J_{max}} \tilde{\psi}_J^{(1)} \star \left(\psi_J^{(3)} * b \right)(r) \right)(\xi), \end{aligned} \tag{92}$$

with $\tilde{\psi}_J^{(1)}(\eta,\xi) = \xi \Delta_\xi^* \tilde{\Psi}_J(\eta,\xi)$. Note that this equation is just a different expression of a well known fact, i.e. the toroidal magnetic field at a certain altitude is solely due to the radial current distributions at that very height. Equation (92) is the starting point of the examples in the next section. It is noteworthy that, from a practical point of view, (92) can successfully be applied if the geomagnetic measurements available are sampled within a comparatively short period of time, i.e. the time-scale under consideration is such that the variations in the satellite's altitude can be neglected to some extend (cf. [27] and [24] for first applications). If the radial variations start to play a role, one can still neglect these variations if the data are appropriately preprocessed, i.e. if suitable geomagnetic field models are subtracted prior to the numerical applications (see e.g. [28]).

6 Applications to Geomagnetic Satellite Data

As examples of the wavelet-Mie-representation of the magnetic field, electric current distributions at satellite altitudes are determined from data sets of vectorial MAGSAT and CHAMP data. The method is based on our considerations in Section 5, especially Equation (92). The current distributions under consideration are due to ionospheric F region currents which are extensively treated in the literature (see [29] and the references therein).

The data sets used in the first example are similar to those used by Olsen [29] for a spherical harmonic approach to the Mie-representation and have kindly been made available by him. MAGSAT was orbiting the Earth in a Sun synchronous orbit thus acquiring only data at dawn and dusk local times. Neglecting the variations in altitude of the MAGSAT satellite, one month of MAGSAT data (centered at March 21, 1980) is transformed to geomagnetic components and is then averaged onto the equiangular longitude-latitude grid (90×90 grid points) proposed in [10], which has then been used to discretize the convolution integrals. This averaging process is performed using a robust Tuckeys biweight method (cf. [19]). The dusk and dawn data are treated separately such that two separate data sets are obtained. Prior to the averaging process a geomagnetic field model (GSFC(12/83) up to degree and order 12) due to [21] is subtracted from the measurements in order to avoid spurious effects due to the neglected altitude variations (cf. [29]).

According to Equation (92) the radial current distribution at a fixed height can be calculated from the wavelet coefficients of the toroidal field at that altitude, i.e. $\left(\psi_J^{(3)} * b\right)(r)$. As regards the present example, we calculate these coefficients by means of spherical vectorial cubic polynomial (CuP) wavelets up to scale 5 from the evening data set. Then, in a second step, these coefficients are utilized to calculate the corresponding radial current distribution. Figure 2 shows the reconstruction of the radial current density $J_{rad} = (\xi \cdot j_{rad}(\xi))$ (Note that, for enhancing the visible features, the colorscale has been driven in saturation, i.e. though there are currents with absolute values larger than 100 nano Amperes per meter squared (nA/m^2) we use a colorbar ranging from -100 to 100 nA/m^2).

The largest radial current densities ($|J_{rad}| \lesssim 150$ nA/m^2) are present in the polar regions. In agreement with the results in [29] the main current flow in the polar cap is directed into the ionosphere ($J_{rad} > 0$) during evening. At the poleward boundary of the polar oval the currents flow out of the ionosphere while the main current direction is into the ionosphere at the equatorward boundary. At the magnetic dip equator one realizes comparatively weak upward currents ($|J_{rad}| \lesssim 25$ nA/m^2) accompanied by even weaker downward currents at low latitudes. These current distributions are the radial components of the so-called meridional current system of the equatorial electrojet. Figure 3 presents the same results as Figure 2 but in a different projection, thus enabling a better view of the meridional currents. As can be expected from theoretical considerations, the corresponding signatures follow the geomagnetic dip equator.

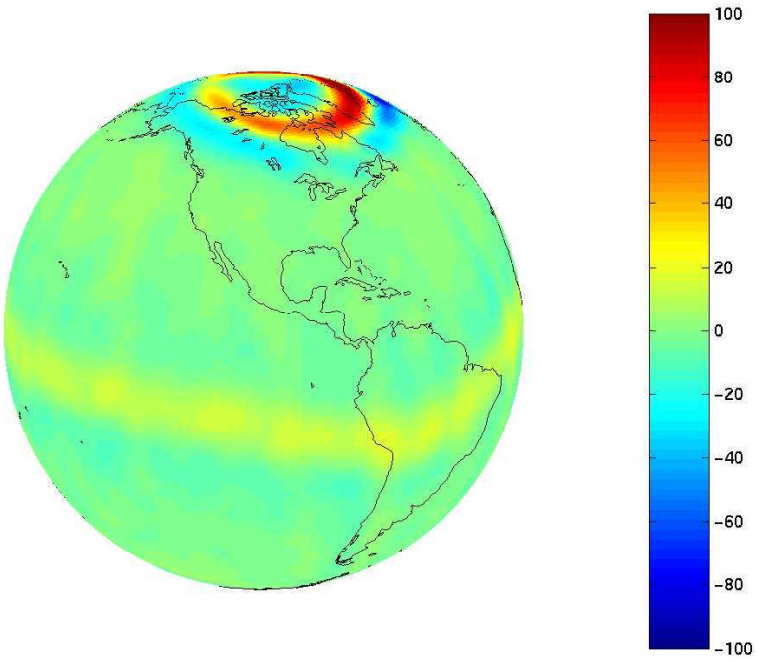

Figure 2: Radial current density during evening local time obtained from a wavelet-Mie-representation of MAGSAT data with vectorial cubic polynomial wavelets up to scale 5. [nA/m^2]

In order to demonstrate the possibility of regional calculations, Figure 4 presents a reconstruction of the radial current systems during dusk local times over the polar region. These results are obtained using vectorial cubic polynomial wavelets of scales 4 and 5 and a data window centered at the geographic north pole with a half angle of 60° as well as

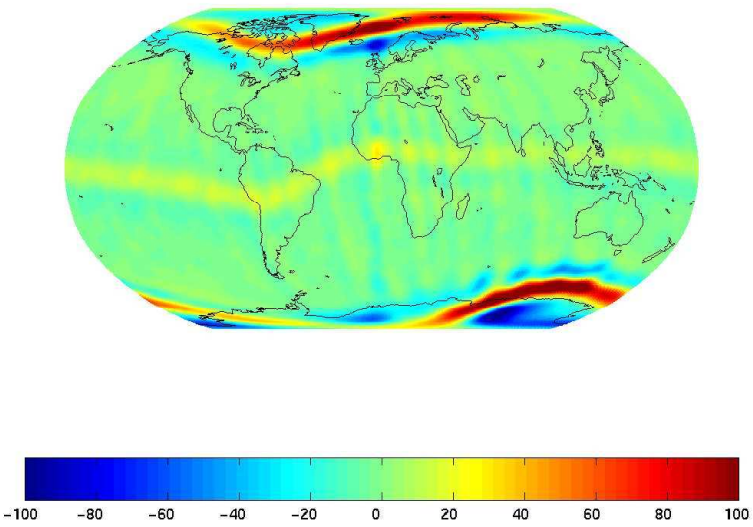

Figure 3: Radial current density during evening local time obtained from a wavelet-Mie-representation of MAGSAT data with vectorial cubic polynomial wavelets up to scale 5. [nA/m^2]

an integration window with the same center but a half angle of 55° (the white border approximately illustrates the extend of the calculation region). The visualization window is a little smaller than the calculation window in order to suppress Gibbs phenomena.

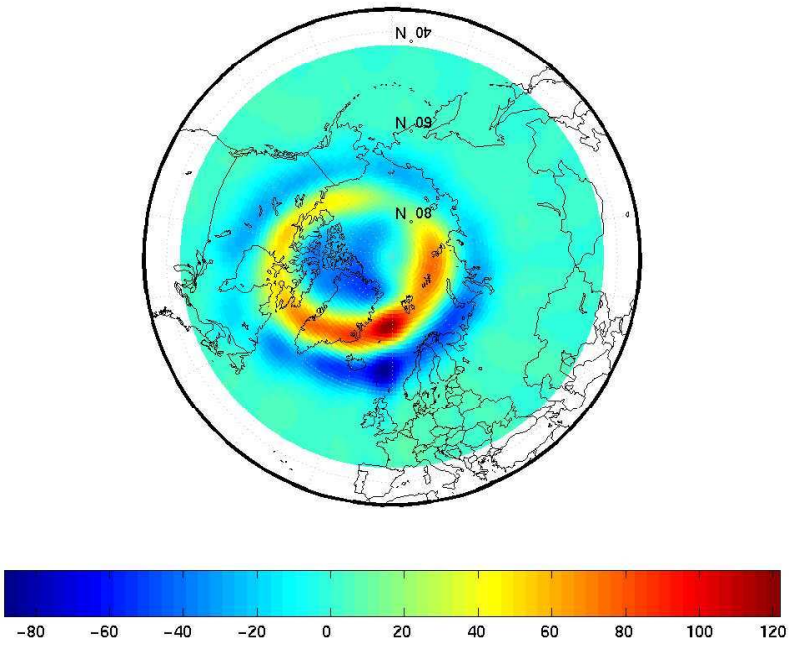

Figure 4: Local reconstruction of radial current density during evening local time obtained from a wavelet-Mie-representation of MAGSAT data with vectorial cubic polynomial wavelets at scales 4 and 5. The white area corresponds to the calculation region. [nA/m^2]

Comparing Figure 4 with Figure 2 shows that the structures of the radial currents are clearly visible though slightly weaker in magnitude. This slight difference is due to

the fact that we have omitted the contributions of wavelet scales up to 3, i.e. features of coarse spatial resolution. The signatures seen in our results are the effects of higher wavelet scales (4 and 5) and consequently are of more or less confined spatial extend. As can be expected from the physical point of view, these are clearly the main radial current contributions in the polar region. The effects of lower scales can be neglected. This, however, demonstrates the regional character of the radial current distributions and suggests the use of space adaptive methods like the one presented here.

The results of the previous example illustrate the geometry of the ionospheric currents at a fixed (magnetic) local time, i.e. the Earth-satellite-Sun geometry was fixed during the process of data accumulation. The reader should be aware of the fact that the current distributions presented in Figures 2, 3 and 4 do not illustrate the global distribution of the radial currents but show a small strip of the currents moving over the Earth (along longitude) during the course of the day. This is because ionospheric current systems are not properly described in Earth-fixed coordinate systems like geographic longitude and latitude. Since the conductance of the ionosphere is varying with the influence of the Sun, the magnetic field induced by ionospheric currents is linked to the position of the Sun and the distance of the observing satellite to the geomagnetic equator. Consequently, a Sun-fixed reference frame should rather be used to parameterize ionospheric currents. The Very advantages in that sense is the coordinate system of magnetic local time $MLT \in [0, 24]$ (instead of longitude) and quasi dipole latitude $QDlat \in [-90, 90]$. The magnetic local time thereby denotes the relative position of the satellite with respect to the magnetic field and the Sun, while the quasi dipole latitude gives the relative position of the satellite with respect to the geomagnetic equator. For more information on these coordinate systems the reader might consult [22] and the references therein. In order to use MLT and QDlat as a parametrization one needs to utilize geomagnetic data from satellites with polar but not Sun synchronous orbits thus covering the whole span of magnetic local times (i.e. from 0h to 24h). The German geoscientific Satellite CHAMP, operated by the GeoForschungs-Zentrum in Potsdam, Germany, is such a satellite. Among other instruments, the CHAMP satellite is equipped with high precision vector and scalar magnetometers and, in contrast to MAGSAT, covers all magnetic local times within four months. In what follows we present a result calculated by Mayer [26] analyzing a CHAMP data set via a wavelet-Mie-Representation parameterized in QDlat and MLT. Three days of CHAMP vector data (September 10th, 16th and 17th, 2001) are used. In polar regions these data suffice to cover the whole span of magnetic local times (see [26]). The polar data are transformed to the QDlat-MLT coordinate system and then averaged to an equiangular integration grid using a robust method. A wavelet-Mie-representation is performed over the geomagnetic north pole and the radial current distributions are calculated via Equation (92) from the toroidal magnetic field contribution. Figure 5 shows the resulting radial currents in the northern polar region which are in accordance with the physical models presented in [20] and [11]. This result can now be interpreted as the evolution of the currents' morphology in magnetic local time; for example, it is clearly visible how the currents' polarity changes at the noon-midnight plane.

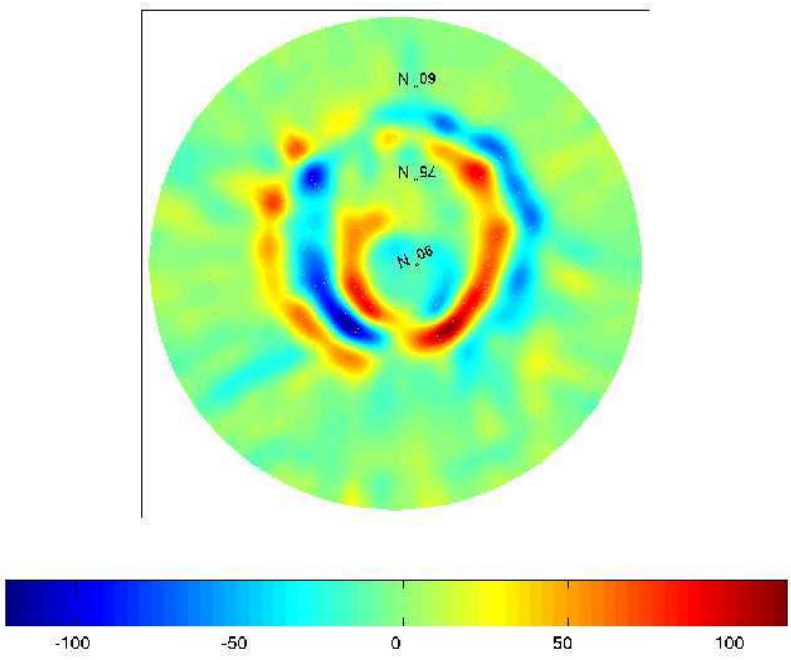

Figure 5: Local reconstruction of radial current density from a wavelet-Mie-representation of CHAMP data in MLT and QDlat, calculated with a cubic polynomial scaling function of scale 6 [nA/m^2]. Figure courtesy of Carsten Mayer [26].

7 Summary and Outlook

The Mie representation for the geomagnetic field has the advantage that it can equally be applied in regions of vanishing as well as non-vanishing electric current densities. The standard method of deriving the Mie representation is given by a spherical harmonic parametrization, i.e. by expanding the corresponding Mie scalars in terms of spherical harmonics. Considering the measurements (magnetic field or currents) to be given in a spherical shell we have presented a wavelet parametrization of the magnetic field and the corresponding electric current densities in Mie representation, i.e. a wavelet-Mie-representation. The use of wavelets as trial functions for field parametrization enables us to cope with electric currents (and corresponding magnetic effects) that vary rapidly with latitude or longitude, or that are confined to certain regions. Consequently, we are able to reflect the various levels of space localization in form of a vectorial multiresolution analysis and can thus take efficient account of the specific concentration of the current densities in space. Using our approach, the direct as well as the inverse geomagnetic source problem admit now a treatment within a vectorial multiscale framework.

Neglecting variations in altitude, we have provided numerical examples that illustrate the multiscale approximation of radial current distributions from sets of vectorial geomagnetic field data from the MAGSAT as well as the CHAMP satellite. Global as well as regional reconstructions of the radial current densities are calculated and demonstrate the functionality of the approach. As regards future studies, the next reasonable step is to incorporate the variations in altitude of the satellite – at least to some extend – since this would allow for the determination of horizontal current distributions, too. Additionally,

– either in studies using synthetic data, or based on satellite data sampled over large time intervals, or using data from multi satellite missions – a simultaneous wavelet parametrization of the poloidal and toroidal magnetic fields from the corresponding electric currents (or vice versa) should be derived in future works.

Acknowledgments

The author thanks Prof. Dr. W. Freeden (TU Kaiserslautern), Dr. C. Mayer (TU Kaiserslautern) and Dr. N. Olsen (Danish Space Research Institute, Copenhagen) for their support, their comments and the many fruitful discussions.

References

[1] G. Backus, *Poloidal and Toroidal Fields in Geomagnetic Field Modeling*, Rev. Geophys., 24 (1986), pp. 75–109.

[2] G. Backus, R. Parker, and C. Constable, *Foundations of Geomagnetism*, Cambridge University Press, Cambridge, 1996.

[3] M. Bayer, S. Beth, and W. Freeden, *Geophysical Field Modelling by Multiresolution Analysis*, Acta Geod. Geoph. Hung., 33 (1998), pp. 289–319.

[4] M. Bayer, W. Freeden, and T. Maier, *A Vector Wavelet Approach to Iono- and Magnetospheric Geomagnetic Satellite Data*, J. of Atmospheric and Solar-Terrestrial Physics, 63 (2001), pp. 581–597.

[5] S. Beth, *Multiscale Approximation by Vector Radial Basis Functions on the Sphere*, PhD thesis, Geomathematics Group, Department of Mathematics, University of Kaiserslautern, 2000.

[6] C. Chui, *An Introduction to Wavelets*, Academic Press, 1992.

[7] I. Daubechies, *The Wavelet Transform, Time-Frequency Localization and Signal Analysis*, IEEE Trans. Inform. Theory, 36 (1990), pp. 961–1005.

[8] P. Deuflhard, *On Algorithms for the Summation of Certain Special Functions*, Computing, 17 (1976), pp. 37–48.

[9] E. Donovan, *Modeling the Magnetic Effects of Field-aligned Currents*, J. Geophys. Res., 98 (1993), pp. 529–543.

[10] J. Driscoll and D. Healy, *Computing Fourier Transforms and Convolutions on the 2-Sphere*, Adv. Appl. Math., 15 (1994), pp. 202–250.

[11] U. Engels and N. Olsen, *Computation of magnetic fields within source regions of ionospheric and magnetospheric currents*, J. Atmos. Sol.-Terr. Phy., 60 (1998), pp. 1585–1592.

[12] W. Freeden, *On Approximation by Harmonic Splines*, Manuscr. Geod., 6 (1981), pp. 193–244.

[13] ——, *Multiscale Modelling of Spaceborne Geodata*, B.G. Teubner, Stuttgart, Leipzig, 1999.

[14] W. Freeden and T. Gervens, *Vector Spherical Spline Interpolation - Basic Theory and Computational Aspects*, Math. Meth. in the Appl. Sci., 16 (1993), pp. 151–183.

[15] W. Freeden, T. Gervens, and M. Schreiner, *Constructive Approximation on the Sphere (With Applications to Geomathematics)*, Oxford Science Publications, Clarendon, 1998.

[16] W. Freeden and U. Windheuser, *Spherical Wavelet Transform and Its Discretization*, Adv. Comput. Math., 5 (1996), pp. 51–94.

[17] ——, *Combined Spherical Harmonic and Wavelet Expansion – a Future Concept in Earths Gravitational Potential Determination*, Appl. Comput. Harm. Anal., 4 (1997), pp. 1–37.

[18] G. Gerlich, *Magnetfeldbeschreibung mit verallgemeinerten poloidalen und toroidalen Skalaren*, Z. Naturforsch., 8 (1972), pp. 1167–1172.

[19] R. Hogg, *An introduction to robust estimation*, in Robustness in Statistics, G. Launer and R. Wilkinson, eds., San Diego, Califonia, 1979, Academic, pp. 1–17.

[20] T. Iijima and A. Potemra, *Large-scale Characteristics of Field-aligned Currents Associated with Substorms*, J. Geophys. Res., 90 (1978), pp. 2593–2598.

[21] R. Langel and R. Estes, *The near-Earth magnetic field at 1980 determined from MAGSAT data*, J. Geophys. Res., 90 (1985), pp. 2495–2510.

[22] R. Langel, N. Olsen, and T. Sabaka, *A Comprehensive Model of the Near-Earth Magnetic Field: Phase 3*, Tech. Report TM-2000-209894, NASA, 2000.

[23] R. Langel, T. Sabaka, R. Baldwin, and J. Conrad, *The near-Earth magnetic field from magnetospheric and quiet-day ionospheric sources and how it is modeled*, Phys. Earth Planet. Inter., 98 (1996), pp. 235–267.

[24] T. Maier, *Multiscale Geomagnetic Field Modeling from Satellite Data – Theoretical Aspects and Numerical Applications*, PhD thesis, Department of Mathematics, University of Kaiserslautern, 2003. urn:nbn:de:bsz:386-kluedo-15533.

[25] S. Maus, *New Statistical Methods in Gravity and Magnetics*, Habilitation, Gemeinsame Naturwissenschaftliche Fakultät der Technischen Universität Carolo-Wilhelmina zu Braunschweig, 2001.

[26] C. Mayer, *Wavelet Modelling of Ionospheric Currents and Induced Magnetic Fields From Satellite Data*, PhD thesis, Department of Mathematics, University of Kaiserslautern, 2003. urn:nbn:de:bsz:386-kluedo-15533.

[27] C. Mayer and T. Maier, *Multiscale Determination of Radial Current Distribution from CHAMP FGM-Data*, in First CHAMP Mission Results for Gravity, Magnetic and Atmospheric Studies, Springer, 2003, pp. 339–345.

[28] N. Olsen, *A new tool for determining ionospheric currents from magnetic satellite data*, Geophys. Res. Lett., 24 (1996), pp. 3635–3638.

[29] ——, *Ionospheric F region currents at middle and low latitudes estimated from MAGSAT data*, J. Geophys. Res., A, 3 (1997), pp. 4563–4576.

[30] A. Richmond, *The Computation of Magnetic Effects of Field-Aligned Magnetospheric Currents*, J. Atmosph. and Terrestrial Physics, 36 (1974), pp. 245–252.

[31] P. Ritter, A. Viljanen, H. Luehr, O. Amm, and N. Olsen, *Ionospheric currents from CHAMP magnetic field data – comparison with ground based measurements*, in First CHAMP Mission Results for Gravity, Magnetic and Atmospheric Studies, C. Reigber, H. Luehr, and P. Schwintzer, eds., Heidelberg, New York, 2003, Springer, pp. 346–352.

[32] B. Schmitt, *The poloidal-toroidal representation of solenoidal fields in spherical domains*, Analysis, 15 (1995), pp. 257–277.

[33] L. Shure, R. Parker, and G. Backus, *Harmonic splines for geomagnetic modelling*, Phys. Earth Planet. Inter., 28 (1982), pp. 215–229.

[34] D. Stern, *Representation of magnetic fields in space*, Rev. Geophys., 14 (1976), pp. 199–214.

[35] J. Waterman, F. Christiansen, V. Popov, P. Stauning, and O. Rasmussen, *Field-aligned currents inferred from low-altitude earth-orbiting satellites and ionospheric currents inferred from ground-based magnetometers – do they render consistent results?*, in First CHAMP Mission Results for Gravity, Magnetic and Atmospheric Studies, C. Reigber, H. Luehr, and P. Schwintzer, eds., Heidelberg, New York, 2003, Springer, pp. 361–368.

Folgende Berichte sind erschienen:

2003

Nr. 1 S. Pereverzev, E. Schock.
On the adaptive selection of the parameter in regularization of ill-posed problems

Nr. 2 W. Freeden, M. Schreiner.
Multiresolution Analysis by Spherical Up Functions

Nr. 3 F. Bauer, W. Freeden, M. Schreiner.
A Tree Algorithm for Isotropic Finite Elements on the Sphere

Nr. 4 W. Freeden, V. Michel (eds.)
Multiscale Modeling of CHAMP-Data

Nr. 5 C. Mayer
Wavelet Modelling of the Spherical Inverse Source Problem with Application to Geomagnetism

Nr. 6 M.J. Fengler, W. Freeden, M. Gutting
Darstellung des Gravitationsfelds und seiner Funktionale mit Multiskalentechniken

Nr. 7 T. Maier
Wavelet-Mie-Representations for Soleniodal Vector Fields with Applications to Ionospheric Geomagnetic Data

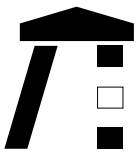

TECHNISCHE UNIVERSITÄT
KAISERSLAUTERN

Informationen:

Prof. Dr. W. Freeden
Prof. Dr. E. Schock
Fachbereich Mathematik
Technische Universität Kaiserslautern
Postfach 3049
D-67653 Kaiserslautern
E-Mail: freeden@mathematik.uni-kl.de
schock@mathematik.uni-kl.de